

MICROLENSING CHARACTERIZATION OF WIDE-SEPARATION PLANETS

CHEONGHO HAN^{1,2}, B. SCOTT GAUDI³, JIN H. AN⁴, AND ANDREW GOULD²*Draft version July 15, 2018*

ABSTRACT

With their excellent photometric precision and dramatic increase in monitoring frequency, future microlensing survey experiments are expected to be sensitive to very short time-scale, isolated events caused by free-floating and wide-separation planets with mass as low as a few lunar masses. The scientific value of these detections would be greatly enhanced if their nature (bound or unbound) could be accurately characterized, and if the planet masses could be measured. We estimate the probability of measuring the Einstein radius θ_E for bound and free-floating planets; this is one of the two additional observables required to measure the planet mass. We carry out detailed simulations of the planetary events expected in next-generation surveys and estimate the resulting uncertainty in θ_E for these events. We show that, for main-sequence sources and Jupiter-mass planets, the caustic structure of wide-separation planets with projected separations of $\lesssim 20$ AU substantially increases the probability of measuring the dimensionless source size and thus determining θ_E compared to the case of unbound planets. In this limit where the source is much smaller than the caustic, the effective cross-section to measure θ_E to 10% is $\sim 25\%$ larger than the full width of the caustic. Measurement of the lens parallax is possible for low-mass planetary events by combined observations from the ground and a satellite located in an L2 orbit; this would complete the mass measurements for such wide-separation planets. Finally, short-duration events caused by bound planets can be routinely distinguished from those caused by free-floating planets for planet-star separations $\lesssim 20$ AU from either the deviations due to the planetary caustic or (more often) the low-amplitude bump from the magnification due to the parent star.

Subject headings: gravitational lensing – planetary systems – planets and satellites: general

1. INTRODUCTION

Microlensing experiments were originally proposed to search for Galactic dark matter in the form of massive compact objects (MACHOs) (Paczyński 1986). However, microlensing developed several other applications including the detection and characterization of extrasolar planets (Mao & Paczyński 1991; Gould & Loeb 1992). Recently, Bond et al. (2004) reported the first clearcut microlensing detection of an exoplanet.

Microlensing planet searches currently operate in the survey/follow-up mode. Large areas of the sky are sparsely monitored by survey collaborations (Alcock et al. 1996; Udalski et al. 2001; Bond et al. 2002) to detect ongoing microlensing events arising from normal stars. These events are alerted in real-time before the event peak, and then individually followed-up with the dense sampling needed to detect the short-duration (about a day for a Jupiter-mass planet and a few hours for an Earth-mass planet) perturbation to the primary lightcurve caused by a planetary companion to the primary lens (Albrow et al. 1998; Rhee et al. 2000; Yoo et al. 2004b). One limitation of this type of planet search strategy, however, is that events are only efficiently followed when the source is located within the Einstein ring radius of the primary. Generally, such source positions are only sensitive to planets with separations located within a certain range of distances from their host stars. Planets in this so called ‘lensing zone’ have separations in the range of $0.6 \lesssim s \lesssim 1.6$, where s is the projected

star-planet separation normalized by the Einstein ring radius. For a typical Galactic bulge event with a lens and a source located at $D_{ol} = 6$ kpc and $D_{os} = 8$ kpc, respectively, the Einstein ring has a radius of

$$r_E \sim 2 \text{ AU} \left(\frac{M}{0.3 M_\odot} \right)^{1/2}, \quad (1)$$

where M is the primary-star mass, and thus current microlensing planet searches are primarily sensitive to planets in the range of projected physical separations, r_\perp , of $1 \text{ AU} \lesssim r_\perp \lesssim 5 \text{ AU}$. Furthermore, because the follow-up is generally done with small field-of-view instruments, the events must be monitored sequentially. As a result, only a few events can be followed at any given time, and it is difficult to achieve the requisite temporal sampling on a sufficient number of events to detect short-duration, low-probability events such as those caused by low-mass or large-separation planets.

These limitations can be overcome with the advent of future lensing experiments that use very large-format imaging cameras to survey wide fields continuously at high cadence. These next-generation surveys dispense with the alert/follow-up mode of searching for planets, and instead simultaneously obtain densely-sampled lightcurves of all microlensing events in their field-of-view (FOV). Because all the stars in the field are monitored continuously regardless of whether they are being lensed or not, planets can be detected at very large projected separations when the primary star is not significantly magnifying the source, and indeed even when the signature of the primary is absent. Therefore these surveys are expected to be sensitive to both wide-separation (Di Stefano & Scalzo 1999a,b) and even free-floating (Bennett & Rhee 2002; Han & Kang 2003) planets. Such planet populations are difficult or impossible to probe by other planet search techniques. Several such high-frequency experiments in space and on the ground have al-

¹ Department of Physics, Institute for Basic Science Research, Chungbuk National University, Chongju 361-763, Korea

² Ohio State University, Department of Astronomy, Columbus, OH 43210

³ Harvard-Smithsonian Center for Astrophysics, 60 Garden St., Cambridge, MA 02138

⁴ Institute of Astronomy, University of Cambridge, Madingley Road, Cambridge CB3 0HA, UK

Electronic address: cheongho@astroph.chungbuk.ac.kr, sgaudi@cfa.harvard.edu, jin@frequency.exploratorium.edu

ready been proposed or are being seriously considered. The proposed space microlensing missions of *Galactic Exoplanet Survey Telescope (GEST*, Bennett & Rhie 2002) and *Joint Dark Energy Exoplanet Mission (JDEEM)* are designed to continuously monitor $\sim 10^8$ Galactic bulge main-sequence stars with $\sim 1\%$ photometric precision and a frequency of several times per hour by using a 1–2 m aperture space telescope. Detailed simulations of the outcomes of a ground-based high-frequency experiment using a network of 2 m-class telescopes are being carried out by Gaudi, Han, & Gould (2004).

Although efficient in detecting planets, the microlensing method suffers the shortcoming that the mass of the detected planet is generally poorly constrained. Analysis of the planet-induced perturbation automatically yields the planet-star mass ratio $q = m_p/M$, but the stellar mass is unknown due to the degeneracy of the physical lens parameters in the principal lensing observable. This degeneracy arises because among the three observables related to the physical parameters of the lens, the Einstein timescale t_E , the angular Einstein radius θ_E , and the Einstein ring radius projected onto the observer plane \tilde{r}_E , only t_E is routinely measurable from the lensing light curve. These three observables are related to the underlying physical lens parameters of the mass M , relative lens-source parallax $\pi_{\text{rel}} = \text{AU} (D_{ol}^{-1} - D_{os}^{-1})$, and proper motion μ_{rel} , by

$$t_E = \frac{\theta_E}{\mu_{\text{rel}}}, \quad \theta_E = \sqrt{\frac{4GM\pi_{\text{rel}}}{c^2 \text{AU}}}, \quad \tilde{r}_E = \sqrt{\frac{4GM \text{AU}}{c^2 \pi_{\text{rel}}}}. \quad (2)$$

For the unique determination of the planet mass, one must, therefore, measure the other two observables of θ_E and \tilde{r}_E . Once θ_E and \tilde{r}_E are known, the lens mass is determined by

$$M = \left(\frac{c^2}{4G} \right) \tilde{r}_E \theta_E. \quad (3)$$

There have been several methods proposed to determine the masses of planets detectable by future lensing experiments. Bennett & Rhie (2002) pointed out that for some events with detected planets, the proposed space lensing mission would detect enough light from the lens star to determine its spectral type and so infer the mass. However, no more than $\sim 1/3$ of lenses are bright enough to be so detected. A more direct method of determining masses of bound planets was proposed by Gould, Gaudi, & Han (2003). They first demonstrated that the precision and sampling of the space observations will be sufficient to routinely detect one projection of the vector quantity⁵ π_E from the primary event. They then demonstrated that a second projection of π_E could be measured by combining observations from a satellite in an L2 orbit with ground-based observations. For this setup, an Earth-satellite baseline of $d_{\text{sat}} \sim 0.005$ AU is sufficient to routinely detect the difference in the peak time of the planetary perturbation as seen from the Earth and satellite for low-mass planets. The difference can then be combined with the known Earth-satellite projected separation to measure the second projection of π_E . The two projections of π_E yield the magnitude of \tilde{r}_E . Moreover, for terrestrial planets with mass ratio $q \sim 10^{-5}$, the Einstein ring radii $\theta_{E,p} = q^{1/2} \theta_E$ is of order the angular source size θ_* of a typical (main-sequence) source. Therefore, the magnification pattern arising from the planet typically has structure on the scale of the source size, which gives rise to finite-source effects on the perturbation lightcurve. From these effects, it

⁵ The vector $\pi_E = \text{AU}/\tilde{r}_E$ has the magnitude of \tilde{r}_E and the direction of relative source-lens proper motion.

would be possible to measure $\rho_* = \theta_*/\theta_E$. The angular size θ_* can be determined from its dereddened color and magnitude using an empirically-calibrated color-surface brightness relation. Thus a measurement of ρ_* can be used to infer θ_E and thus complete the mass measurement via equation (3).

Han et al. (2004) demonstrated that the same observational setup discussed by Gould, Gaudi, & Han (2003) to determine the mass of bound planets can also be used to determine the masses of free-floating planets. The principles are generally the same, however the primary difference is the lack of structure in the planet deviation caused by the small caustic residing at the center of the planet's Einstein ring that exists for bound planets. This lack of structure is beneficial because it allows one to unambiguously determine both components of π_E from the planetary event itself. However, it also implies that the cross section for significant finite-source effects is much smaller than in the bound-planet case, for which the caustic structure is significantly extended. Essentially, it is only possible to detect finite-source effects, and so measure θ_E , for those events in which the source star transits the planet. The angular radius θ_* of a typical main-sequence source star in units of the Einstein ring radius $\theta_{E,p}$ of a planet is,

$$\rho_{*,p} \equiv \frac{\theta_*}{\theta_{E,p}} \sim 0.6 \left(\frac{m_p}{M_\oplus} \right)^{-1/2}, \quad (4)$$

where m_p is the mass of the planet, and we have assumed $\theta_* \simeq 0.6 \mu\text{as}$, which is typical for main-sequence sources in the bulge, and $\pi_{\text{rel}} \simeq 42 \mu\text{as}$ (i.e. $D_{ol} = 6$ kpc and $D_{os} = 8$ kpc). Therefore, mass measurements are only routine for planets with masses for which $\rho_{*,p} \gtrsim 1$, i.e., essentially $m_p \lesssim 0.3 M_\oplus$, and are less common for larger mass planets.

Events caused by wide-separation planets have similarities to events produced by both free-floating planets as well as events caused by planets in the lensing zone. The gross structure of events caused by wide-separation planets is similar to that of free-floating planets, and thus the mass of the planet can be determined in a similar way. For wide-separation planetary events, however, the primary (parent star) provides a shear at the location of the planet of $\gamma = s^{-2}$. This shear produces a caustic of angular width $\sim 4\gamma\theta_{E,p}$ near the location of the planet. This small caustic can cause anomalies near the peak of the light curves. Han & Kang (2003) pointed out that these anomalies can be used to distinguish events caused by bound planets from those caused by free-floating planets. In addition, this extended caustic structure increases the cross-section for significant finite source-size effects, thereby increasing the fraction of events for which it is possible to measure $\theta_{E,p}$ (and thus the planet mass) relative to the unbound case.

In this paper, we present a comprehensive discussion of the ability of microlensing to characterize wide-separation planets, consolidating and augmenting the studies of Gould, Gaudi, & Han (2003), Han et al. (2004), and Han & Kang (2003). We consider the ability of microlensing to distinguish free-floating planets from bound planets, as well to measure the mass and projected physical separation of wide-separation planets, as a function of these parameters. The paper is organized as follows. In § 2, we discuss the lensing characteristics of wide-separation planetary events. In § 3, we estimate the probability of measuring $\rho_{*,p}$ from future space observations of wide-separation planetary events by performing detailed simulations of these events, and assessing the resulting uncertainties in $\rho_{*,p}$. In § 4, we

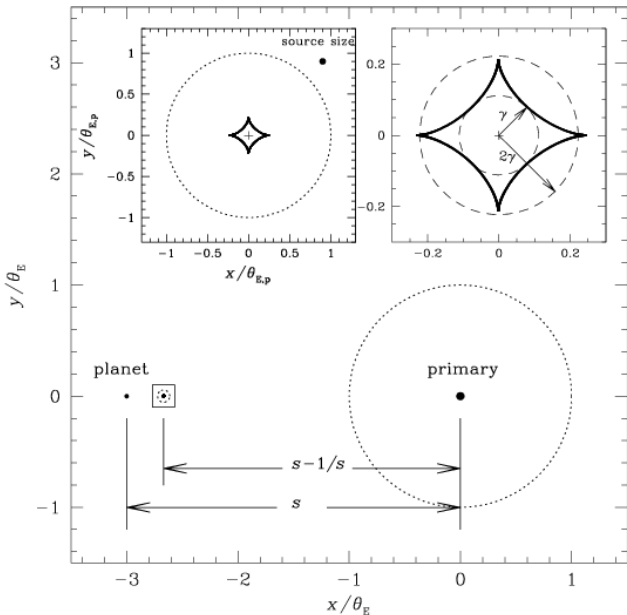


FIG. 1.— Lensing geometry of a star with a wide-separation planet. Shown are the locations of the star (at the origin), planet (at $[x, y] = [-3, 0]\theta_E$), and the resulting caustics. The tiny central caustic is located very close to the star, and the planetary caustic is located in the region enclosed by a small box. The upper left inset is a blowup of the region around the planetary caustic. The dotted circles represent the Einstein rings of the individual lens components around their effective lens positions. The upper right inset shows the planetary caustic enclosed by two circles with radii of 1.0γ and 2.0γ , respectively, where γ is the shear. The geometry is for the case in which the planet/star mass ratio is $q = 3 \times 10^{-3}$ and the normalized separation is $s = 3$. The small disk at the upper right corner of the left inset represents the size of a source star with a radius $R = 1.0 R_\odot$ at $D_{os} = 8$ kpc. For the lens, we assume $M = 0.3 M_\odot$ and $D_{ol} = 6$ kpc, and thus the angular Einstein radius is $\theta_E = 0.32$ mas. Note that the axes of the main panel are scaled by the combined Einstein radius (θ_E), while the axes of the insets are scaled by the Einstein ring radius of the planet ($\theta_{E,p} = \sqrt{q}\theta_E$).

summarize the ability of microlensing to characterize wide-separation planets, as well as discuss methods of distinguishing planetary lensing events caused by free-floating planets from those caused by wide-separation planets. We conclude in § 5.

Throughout this paper, we assume that the lens system (star, planet, or both) is located at $D_{ol} = 6$ kpc, and that the source is a solar-type star with radius $R = R_\odot$ located at $D_{os} = 8$ kpc. Thus $\theta_* = 0.58$ μas and $\pi_{\text{rel}} = 41.7$ μas. The relative proper motion is assumed to be $\mu_{\text{rel}} = 26.0$ km s⁻¹ kpc⁻¹, which yields, for a (star or planet) lens of mass M , an event timescale of $t_E \simeq 38.8$ days $(M/M_\odot)^{1/2}$, an angular Einstein ring radius of $\theta_E \simeq 582$ μas $(M/M_\odot)^{1/2}$, a projected Einstein ring radius of $\tilde{\theta}_E \simeq 13.9$ AU $(M/M_\odot)^{1/2}$, and a dimensionless source size of $\rho_* \simeq 10^{-3}(M/M_\odot)^{1/2}$. When specified, we assume a primary mass of $M = 0.3 M_\odot$.

2. WIDE-SEPARATION PLANETARY EVENTS

Generally, one can write the mapping from the lens plane to the source plane of N point masses with no external shear or convergence as,

$$\zeta = z - \sum_{j=1}^N \frac{m_j/M}{\bar{z} - \bar{z}_{L,j}}, \quad (5)$$

(Witt 1990), where $\zeta = \xi + i\eta$, $z_{L,j} = x_{L,j} + iy_{L,j}$, and $z = x + iy$ denote the source, lens, and image positions, respectively, \bar{z} denotes the complex conjugate of z , and m_j/M are the mass fractions of the individual lens components ($\sum_j m_j = M$). Here all angles are normalized to the Einstein ring radius θ_E of the total mass of the system M . The lensing process conserves the source surface brightness, and thus the magnifications A_i of the individual images i correspond to the ratios between the areas of the images and the source. For an infinitesimally small source element, this is,

$$A_i = \left| \left(1 - \frac{\partial \zeta}{\partial \bar{z}} \frac{\partial \bar{\zeta}}{\partial z} \right)^{-1} \right|. \quad (6)$$

The total magnification is just the sum over all images, $A = \sum_i A_i$.

For a single lens ($N = 1$), one can easily invert the lens equation to solve for image positions (x, y) and magnifications as a function of the source position (ξ, η). This yields the familiar result that there are two images for every source position $\zeta \neq 0$. These two images have angular separations $\theta \equiv |z - z_L|$ from the lens of $\theta_{\pm} = 0.5[u \pm (u^2 + 4)^{1/2}]$, where $u \equiv |\zeta - z_L|$. The image $\theta_+ > 1$ ($\theta_- < 1$) is often referred to as the major (minor) image

A planetary lens is described by the formalism of a binary ($N = 2$) lens. In this case, the lens equation cannot be inverted algebraically. However, it can be expressed as a fifth-order polynomial in z and the image positions are then obtained by numerically solving the polynomial (Witt & Mao 1995). One important characteristic of binary lensing is the formation of caustics, which represent the set of source positions at which the magnification of a point source becomes infinite. The number and size of these caustics depends on the projected separation s and the mass ratio q .

One can think of a wide-separation planet with $s \gg 1$ and $q \ll 1$ as a perturbation to the major image produced by the primary. The location of the major image produced by the primary is $\theta_+ = 0.5[u + (u^2 + 4)^{1/2}]$, and therefore a planet separated by s from its parent star will produce a ‘planetary’ caustic on the star-planet axis at an angular separation from its parent star of $\hat{s} = s - 1/s$ (see Fig. 1). In addition, there will be a second, smaller ‘central’ caustic located near the star (Griest & Safizadeh 1998). By choosing the origin in the image plane as the position of the planet, the origin in the source plane as the point on the star-planet axis with an angular separation \hat{s} from the primary, and then normalizing all angles to the Einstein ring of the secondary, it is straightforward to show that, in the limit $s \gg 1$ and $q \ll 1$, the binary-lens equation becomes

$$\hat{\zeta} = \hat{z} - \frac{1}{\hat{\bar{z}}} + \gamma \hat{\bar{z}}, \quad (7)$$

(Dominik 1999). Here $\gamma = s^{-2}$ is the shear and the notations with upper ‘hat’ mark represent the length scales normalized by the Einstein radius corresponding to m_2 , e.g. $\hat{z} = z(\theta_E/\theta_{E,2})$. This is the well-known Chang & Refsdal (1979, 1984) lens. In its range of validity, equation (7) implies that if the planetary separation is sufficiently wide, the lensing behavior in the region around the planetary Einstein ring can be approximated as a single point-mass lens superimposed on a uniform background shear γ . The caustics created by a Chang-Refsdal lens with $\gamma < 1$ have an asteroid shape (see Fig. 1) with full width along the star-planet axis and height normal to the planet-star

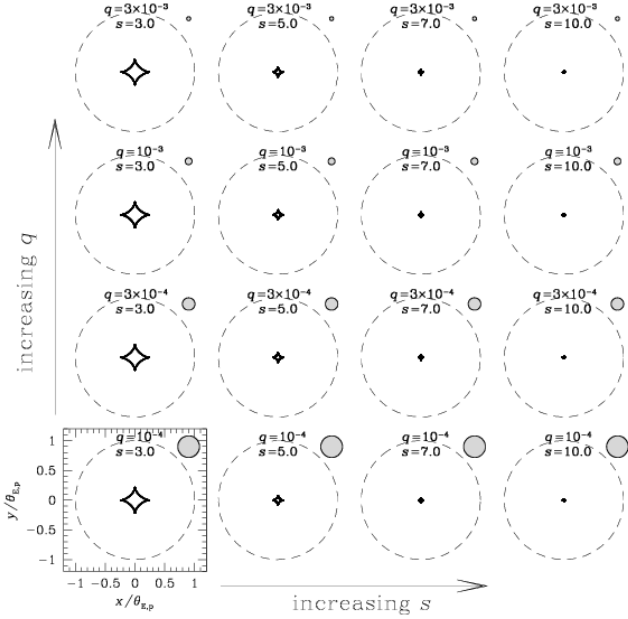


FIG. 2.— Variations of the caustic and source sizes relative to the size of the planetary Einstein ring of wide-separation planets with various mass ratios relative to and separations from the primary star. In each panel, the diamond-shaped figure is the planetary caustic, the dashed circle represents the Einstein ring of the planet, and the shaded small circle in the upper right corner represents the size of the source star relative to the planetary Einstein ring. Panels are arranged so that the separation and mass ratio are increasing along the abscissa and ordinate, respectively. The assumed lens geometry is that the lens and source star are located at $D_{ol} = 6$ kpc and $D_{os} = 8$ kpc, respectively, and the source star has a physical radius of $R_* = 1.0R_\odot$.

axis of, respectively,

$$2a_{C-R} = \frac{4\gamma}{\sqrt{1-\gamma}}, \quad 2b_{C-R} = \frac{4\gamma}{\sqrt{1+\gamma}}. \quad (8)$$

Thus, as the separation between the star and planet increases, the size of the caustic shrinks approximately as $1/s^2$, and both lens components tend to behave as if they are two independent single lenses.

For the applications discussed here, the angular size of the source is typically non-negligible relative to the Einstein ring of the secondary, $\theta_{E,p}$. Therefore, finite source effects must be taken into account. It is precisely these finite source effects that allows one to measure $\theta_{E,p}$. The magnification of a finite source is computed by the intensity-weighted magnification averaged over the source star flux, i.e.,

$$A_{fs}(\zeta) = \frac{\int_S I(\zeta') A(\zeta + \zeta') d\zeta'}{\int_S I(\zeta') d\zeta'}, \quad (9)$$

where A denotes the magnification of the corresponding point source, ζ is the vector position of the center of the source, ζ' is the displacement vector of a point on the source star surface with respect to the source star's center, and the two-dimensional integral is over the source-star surface S . For a source with uniform surface brightness, the computation can be reduced from a two-dimensional to a one-dimensional integral using the Generalized Stokes's theorem (Gould & Gaucherel 1997; Dominik 1998). The finite-source effect becomes important when the source passes over a magnification pattern with small-scale structure or crosses the caustics. Because wide-separation planetary events have such

extended magnification structures (i.e., the planetary caustics), the chance to measure $\rho_{*,p}$ is expected to be higher compared to the case of free-floating planet events.

In Figure 2, we show how the relative caustic and source sizes vary with respect to the Einstein radius for wide-separation planets with various mass ratios relative to and separations from the primary star, using the full binary-lens formalism. For a fixed angular source size θ_* , the normalized source size $\rho_{*,p}$ becomes smaller with increasing planet/star mass ratio (as $\rho_{*,p} \propto q^{-1/2}$). However, in the parameter regimes shown in the figure, the Chang-Refsdal approximation is excellent, and therefore the size of the caustic in units of $\theta_{E,p}$ depends almost solely on s . Thus, as the separation increases, the caustic width decreases as $\sim 4\gamma \propto s^{-2}$.

3. PROBABILITY OF MEASURING $\theta_{E,p}$

We now address the question of what fraction of wide-separation planetary events in future lensing experiments will yield an accurate measurement of $\theta_{E,p}$. We estimate the probability, P , that a given wide-separation planetary event will exhibit substantial finite source effects and so allow the measurement of $\rho_{*,p}$ to a given accuracy (in turn yielding $\theta_{E,p}$). In particular, we are interested in how the existence of the caustic created by the shear from the primary increases the probability relative to a free-floating planet event with similar lensing characteristics.

In order to estimate the probability P , we carry out detailed simulations of wide-separation planetary events and estimate the uncertainties of $\rho_{*,p}$ determined from simulated light curves. Although wide-separation planetary events are reasonably well-described by the Chang-Refsdal approximation, in order to make our results fully general, we will carry out our simulations using the full binary-lens formalism. However, we will use the Chang-Refsdal approximation to aid in the interpretation of our results. The simulations proceed as follows. Planetary microlensing event lightcurves are calculated using equations (5) and (6). The ranges of the planetary separations and mass ratios of the tested events are $2 \leq s \leq 20$ and $10^{-5} \leq q \leq 10^{-2}$, respectively. Finite-source effects are incorporated by computing a one-dimensional line integral along the boundaries of the images, whose positions are obtained by numerically solving the lens equation, and then applying Stokes's theorem. The majority of target stars to be monitored by the proposed space microlensing mission are Galactic bulge main-sequence stars, we therefore assume a solar-type source star with an apparent magnitude of $I \sim 21$. For the space observations, we follow the specification of the *GEST* mission (Bennett & Rhee 2002) and assume that events are monitored with a frequency of $f_{obs} = 5 \text{ hr}^{-1}$ and that a 600-second exposure image is acquired from each observation. We assume a photon acquisition rate of 13 photons/s for an $I = 22$ star.

Once events are produced from the simulation, the uncertainties of the individual fitting parameters (p_i) are determined from each light curve by

$$\sigma_i = \sqrt{c_{ii}}, \quad c = b^{-1}, \quad (10)$$

where c_{ij} is the covariance matrix, and the curvature matrix of the χ^2 surface is defined by

$$b_{ij} = \sum_{k=1}^{N_{\text{obs}}} \frac{\partial F_k}{\partial p_i} \frac{\partial F_k}{\partial p_j} \frac{1}{\sigma_k^2}. \quad (11)$$

Here $F_k(t) = A(t_k)F_S + F_B$ represents the observed flux for each measurement, F_S and F_B are the fluxes of the source and

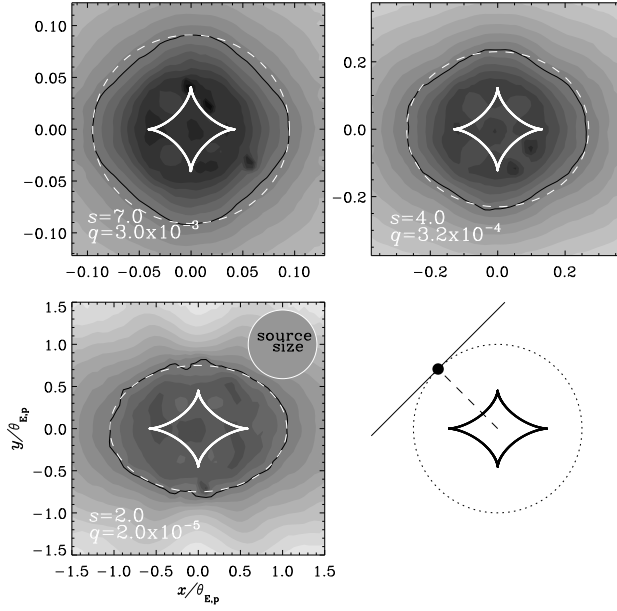


FIG. 3.— Contour maps of the fractional uncertainty $\sigma_{\rho_{*,p}}/\rho_{*,p}$ as a function of the source position relative to the planetary caustic. Each position on the map represents a source trajectory that passes through that position and is normal to the line connecting the position and the caustic center (see the geometry in the lower right panel). For all three presented cases, the source size relative to the caustic size is nearly the same. The dark closed curve in each panel represents the contour at which $\sigma_{\rho_{*,p}}/\rho_{*,p} = 10\%$ and the white dashed curve is the approximation of this contour as an ellipse.

blended light, N_{obs} is the total number of measurements, and σ_k is the measurement error. For planetary lensing, the total number of parameters is 9 including s , q , F_S , F_B , $\rho_{*,p}$, $t_{E,p}$, t_0 , α , and $u_{0,p}$, where we define $t_{E,p}$ as the time required for the source to transit $\theta_{E,p}$, t_0 is the time of the closest approach to the planetary caustic, $u_{0,p}$ is the separation (normalized by $\theta_{E,p}$) at that moment, and α is the orientation angle of the source trajectory with respect to the star-planet axis. According to the luminosity function of the Galactic bulge field (Holtzman et al. 1998), the surface number density of stars with $I \lesssim 24$ is $\sim 5,000 \text{ stars/arcmin}^2 \sim 1.4 \text{ stars/arcsec}^2$, and thus a space mission equipped with a $\sim 1 \text{ m}$ telescope can resolve most neighboring stars. However, since one cannot exclude the possibility of blending by the light from a companion to the source or by the lens itself, we include the blending parameter F_B . For the simulation, we set the blending fraction to be $F_B/F_S = 0.3$. The photometric uncertainty is assumed to be limited by photon statistics and the uncertainties of the fitting parameters are determined from the light curve measured during $-2.0 t_{E,p} \leq t - t_0 \leq 2.0 t_{E,p}$.

As we argued in § 2, the lensing behavior of a wide-separation planet is locally well-described by a single lens with external shear $\gamma = s^{-2}$, i.e. a Chang-Refsdal lens. Therefore, the magnification structure can be described by only two parameters, namely $(\gamma, \rho_{*,p})$, rather than the three parameters (s, q, ρ_*) generically required for full binary lensing. In fact, for $\gamma \ll 1$ ($s \gg 1$), the Chang-Refsdal lens becomes self-similar: when all angles are normalized to 2γ , the magnification pattern is nearly independent of γ . Therefore, the ability to measure $\rho_{*,p}$ depends primarily on the single parameter $\rho_{*,p}/\gamma$. In fact, this scaling breaks down for two reasons. First, as γ approaches unity, the self-similarity of the Chang-

Refsdal lens breaks down. Second, because we are considering a fixed sampling rate, the number of samples per planetary crossing time $t_{E,p} = q^{1/2} t_E$ decreases for smaller-mass planets. Therefore, the error on the light curve fit parameters, which depends on both the magnification structure and the density of data points, formally depends on q as well. However, these two effects are generally sub-dominant, and therefore the dependence on γ or q for fixed $\rho_{*,p}/\gamma$ is relatively weak. We demonstrate this by computing the fractional uncertainty $\sigma_{\rho_{*,p}}/\rho_{*,p}$ as a function of the source positions around the planetary caustic. Figure 3 shows the contour maps of $\sigma_{\rho_{*,p}}/\rho_{*,p}$ for three different combinations of s and q yielding the same ratio of $\gamma/\rho_{*,p}$. In the maps, each position represents a source trajectory that passes through that position and is normal to the line connecting the position and the caustic center (see the geometry illustrated in the lower right panel), and the closed curve drawn by a dark line represents the contour at which $\sigma_{\rho_{*,p}}/\rho_{*,p} = 10\%$. From a comparison of the maps, one finds that the patterns look qualitatively similar despite the great differences in the values of s and q , confirming the argument that the ability to measure $\rho_{*,p}$ depends primarily on $\rho_{*,p}/\gamma$.

A straightforward approach to estimate P would be first to construct maps of $\sigma_{\rho_{*,p}}/\rho_{*,p}$ such as the ones shown in Figure 3 for the various combinations of s and q , second to draw many light curves with various combinations of $u_{0,p}$ and α obtained from one-dimensional cuts through each constructed map, and then to estimate the probability as the ratio between the number of light curves yielding uncertainties smaller than a threshold value out of the total number of tested events. However, we find that this approach is difficult to implement because constructing the large number of high-resolution maps that incorporate finite-source effects demands a large amount of computation time even after the great reduction of finite-source calculations using Stokes's theorem (i.e., from a two-dimensional to a one-dimensional integral). Fortunately, we find that the region where $\rho_{*,p}$ can be measured to a given precision (the effective region) is well confined around the planetary caustic and its boundary is, in general, approximated as an ellipse as illustrated in Figure 3. We therefore estimate P by determining the semi-major, a , and semi-minor, b , axes of the ellipse and then compute the probability, which corresponds to the ratio of the angle-averaged cross-section of the ellipse to the diameter of the planetary Einstein ring⁶, by

$$P = \frac{1}{\pi} \int_0^\pi \sqrt{a^2 \sin^2 \alpha + b^2 \cos^2 \alpha} d\alpha = \frac{2}{\pi} a E(e), \quad (12)$$

where E represents the complete elliptical integral of the second kind and $e = (1 - b^2/a^2)^{1/2}$. Note that, since a and b are in units of $\theta_{E,p}$, the probability is normalized such that P is the

⁶ The approximation of the boundary of the effective region as an ellipse becomes poor as the source size becomes smaller than the caustic size. In the limiting case $\rho_{*,p} \ll \gamma$, the positions at which finite source effects are large (allowing $\rho_{*,p}$ to be effectively measured) are confined to regions near the caustic itself, as well as the protruding region outside of the caustic cusps (the dark shaded regions in Fig. 4). Even in this limiting case, however, we note that the probability P determined by eq. (12) is still a good approximation. This is demonstrated in Fig. 4, in which the light shaded region enclosed by the clover-shaped figure represents the effective region of source trajectories that can pass the dark shaded region, and the dashed circle represents the boundary of the effective region following the ellipse approximation. We find that even in this extreme case, the ratio between the angle-averaged cross-sections of the clover-shaped and circular regions is 0.903, implying that the error in the probability as determined by the ellipse approximation is not important.

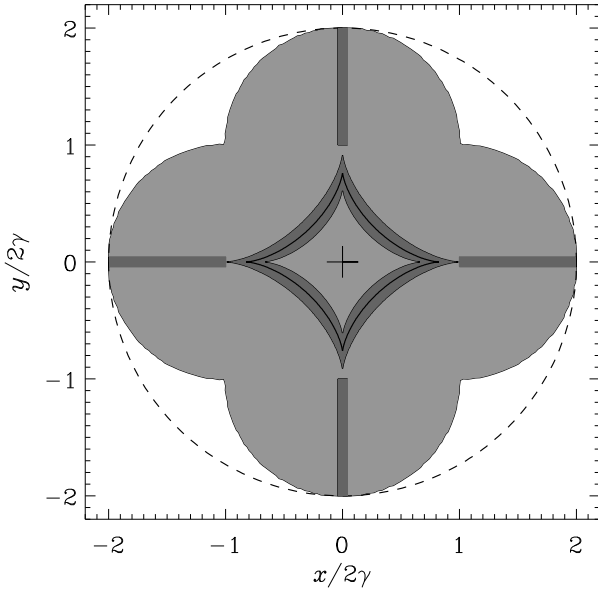


FIG. 4.— Cartoon showing the validity of approximating the effective region for $\rho_{*,p}$ measurement as an ellipse. Here the dark shaded area represents the source positions where, for $\rho_{*,p} \ll \gamma$, finite source effects are large, thus allowing $\rho_{*,p}$ to be effectively measured. The light shaded region enclosed by the clover-shaped figure represent the effective region of source trajectories that pass the dark shaded region, and the dashed circle represents the boundary of the effective region following the ellipse approximation. We note that the cross sections of the dark and light shaded regions are, by definition, same. All lengths are normalized by the caustic size, i.e., 2γ .

fraction of events with $u_{0,p} \leq 1$ that yield a measurement of $\rho_{*,p}$ to a given fractional precision $\sigma_{\rho_{*,p}}/\rho_{*,p}$. Planetary events with $u_{0,p} > 1$ may well be detectable in the next-generation lensing surveys, and thus the fraction of detectable planetary lensing events with a measurement of $\rho_{*,p}$ to a given accuracy is likely to be smaller. We address this point in § 4.

Figure 5 shows the contour map (marked by white contours and grey scales) of the determined probability P as a function of the planetary separation and mass ratio. For the map, the imposed threshold uncertainty is $(\sigma_{\rho_{*,p}}/\rho_{*,p})_{th} = 10\%$. From the probability map, we find two basic regimes. First, in the region of the parameter space where the caustic size is much smaller than the source size, the contribution of the caustic to the probability is not important and the value of P is essentially the same as that of the corresponding free-floating events. Since $\rho_{*,p}$, which is the dominant factor determining P in this region, depends only on the mass ratio and does not depend the separation, the probability distribution is flat as shown in the right lower part of Figure 5. On the other hand, in the region where the caustic size is of the order or larger than the source size, the contribution of the caustic to P becomes important. The caustic size, and thus P , rapidly increase with the decrease of the planetary separation, and this is reflected in the probability distribution trends in the upper left part of Figure 5. We find that the two regions (i.e., source- and caustic-size dominant regions) are divided roughly by the line $\rho_{*,p} = 4\gamma$. Knowing that the relative cross-section for $\rho_{*,p}$ measurement results from the combination of the caustic and normalized source sizes, and keeping the validity of the Chang-Refsdal lensing in mind, we interpret the result by analytically assessing the probability based on the semi-major and semi-minor axes of the effective region as the linear com-

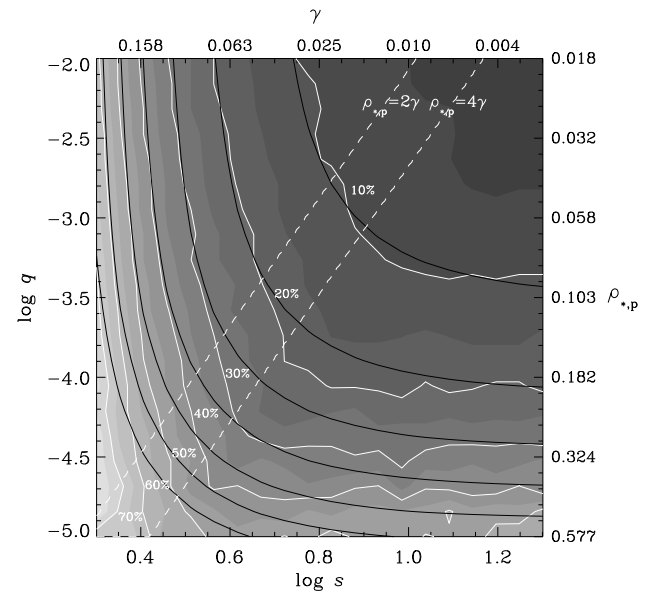


FIG. 5.— Probability P of measuring $\rho_{*,p}$ for wide-separation planetary events as a function of the planetary separation and mass ratio. The adopted threshold uncertainty is $(\sigma_{\rho_{*,p}}/\rho_{*,p})_{th} = 10\%$. The two sets of contours drawn by dark and white lines are based on numerical computations considering the full binary lensing and an analytic treatment using the Chang-Refsdal lensing, respectively (see the text for details). The grey-scale tones show the probability P based on numerical computations: they change for every 5% change of P . The two dashed straight lines represent the positions at which $\rho_{*,p} = 2.0\gamma$ and 4.0γ , respectively.

bination of the Chang-Refsdal caustic size and the normalized source radius, i.e.,

$$\begin{aligned} a &= \mathcal{C}_\gamma a_{C-R} + \mathcal{C}_{\rho_*} \rho_{*,p}, \\ b &= \mathcal{C}_\gamma b_{C-R} + \mathcal{C}_{\rho_*} \rho_{*,p}, \end{aligned} \quad (13)$$

where a_{C-R} and b_{C-R} are defined in equation (8), and \mathcal{C}_γ and \mathcal{C}_{ρ_*} are linear coefficients. In the point-mass limit ($\gamma \ll \rho_{*,p}$), it is known that $\rho_{*,p}$ can be measured only when the lens crosses the source star (Gould & Welch 1996), and thus we set $\mathcal{C}_{\rho_*} = 1.0$. By adjusting \mathcal{C}_γ , we find that $\mathcal{C}_\gamma \sim 2.5$ yields the best-fit probability distribution (marked by dark contours in Fig. 5) to the one based on numerical computations. This implies that in the caustic-dominant regime, the effective cross section of the caustic for a $\rho_{*,p}$ measurement is larger than its full width by $\sim 25\%$, i.e. $a/(4\gamma) \simeq 1.25$.

Translating a measurement of $\rho_{*,p}$ into a measurement of $\theta_{E,p}$ requires knowledge of the angular size of the source θ_* . This can be estimated from the known source color and magnitude as described in Yoo et al. (2004a). Briefly, the process works as follows. The apparent source color and apparent magnitude can be estimated from multicolor photometry taken at several different source magnifications. The dereddened color and magnitude can then be found by comparing to the apparent color and magnitude of nearby stars in the red clump, whose dereddened color and magnitude are known. This assumes that the source star is being seen through the same column of dust as the stars in the red clump. In practice, however, even fairly large differences in the dust column have relatively little effect because the source color and magnitude have opposite effects on the inferred value of θ_* . The angular size θ_* of the source can then be inferred from its color and magnitude using an empirical color-surface brightness rela-

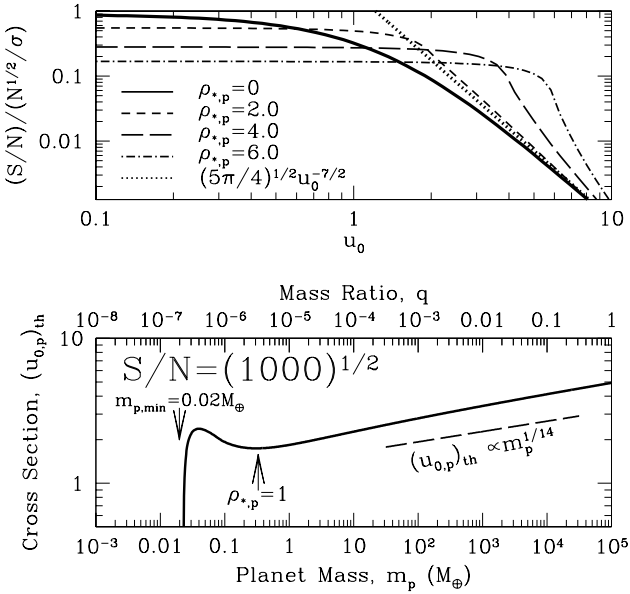


FIG. 6.— Top panel: The curves show the normalized signal-to-noise ratio $(S/N)/(N^{1/2}/\sigma)$, as a function of the impact parameter u_0 , for single lens events with various values of the source size $\rho_{*,p}$ in units of the Einstein ring radius. Here N is the number of points per Einstein crossing time each with fractional precision σ . The solid curve is for a point source ($\rho_{*,p} = 0$), and the dotted curve shows the limiting form for a point source light curve with $u_0 \gg 1$, i.e. eq. (15). Bottom panel: The solid curve shows the cross-section $(u_{0,p})_{th}$ to detect a planet at $S/N \geq (1000)^{1/2}$ as a function of its mass m_p (bottom axis) and mass ratio q (top axis). The long-dashed line shows the scaling $(u_{0,p})_{th} \propto m_p^{1/14}$, which is valid for point sources and $(u_{0,p})_{th} \gg 1$. Also shown are the minimum detectable planet mass, $m_{p,min} \simeq 0.02 M_\oplus$, and the mass at which $\rho_{*,p} = 1$.

tion (e.g. van Belle 1999). The statistical error in the derived value of θ_* from this procedure will likely be dominated by the intrinsic scatter in the empirical color-surface brightness relation, which is currently $\sim 10\%$. Therefore, the error in the inferred value of $\theta_{E,p}$ will be dominated by the error in $\rho_{*,p}$ for $\sigma_{\rho_{*,p}}/\rho_{*,p} \gtrsim 10\%$.

4. CHARACTERIZATION OF WIDE-SEPARATION PLANETS

In this section, we summarize the potential of next-generation microlensing surveys to characterize wide-separation planets, focusing on their ability to distinguish isolated planetary events caused by free-floating planets from those caused by wide-separation planets as a function of the separation of the planets from their host stars. As the formation processes and evolution histories of wide-separation and free-floating planets are believed to be substantially different, unless these two populations of planetary events can be distinguished, it will be difficult to extract useful information about the formation and evolution of these individual planet populations.⁷ We also summarize the capacity of these surveys to measure the masses of the planets through the measurement of θ_E and \tilde{r}_E , as a function of the planet mass and separation.

⁷ In fact, the frequency of bound and free-floating planets must be determined statistically from the ensemble of observed planetary events. As we demonstrate in §4.3, the majority of events from wide planets with $r_\perp \gtrsim 20$ AU will show no signature of the primary, and so it is not generically possible to distinguish between bound and free-floating planets on an event-by-event basis. Therefore, it will be necessary to use those events that are known to be due to bound planets to statistically infer the fraction of events with no signature of a primary that are due to bound planets.

The majority of the calculations in the following sections are independent of the mass of the primary, and so our results are most naturally expressed in terms of their dependence on the planet mass m_p , rather than the planet mass ratio, q . However, to make contact with the results from the previous sections, we will also quote results in terms of q , assuming a primary mass of $M = 0.3 M_\odot$, i.e. $q = 10^{-5}(m_p/M_\oplus)$.

4.1. Cross Section for Detection

We first address the question of the detectability of planets as a function of their mass. For fixed μ_{rel} and π_{rel} , and for identical observational setups, larger-mass planets are detectable to larger planetary impact parameters $u_{0,p}$ because the number of points per crossing time is larger, thereby increasing the S/N . This implies a larger cross section for detection. As the mass ratio decreases, the minimum impact parameter required to produce a lightcurve above a given S/N decreases, thus decreasing the cross-section for detection. Eventually, finite source size effects become important when $\rho_{*,p} \gtrsim 1$. For sufficiently high photometric accuracy, finite source effects can increase the cross section, since the timescale for the event will be set by the crossing time of the source, $t_* \equiv \rho_{*,p}/\mu_{\text{rel}}$, rather than the planetary Einstein crossing time, $t_{E,p}$. Eventually, however, when $\rho_{*,p} \gg 1$ the deviation due to the planet will be completely suppressed, and the planet will be undetectable. To quantify these trends, we determine the expected S/N of an isolated single-lens event,

$$\frac{S}{N} = \frac{N^{1/2}}{\sigma} \left\{ \int d\tau [1 - A_{fs}(\tau; u_{0,p}, \rho_{*,p})^{-1}]^2 \right\}^{1/2}. \quad (14)$$

where N is the number of measurements per planet Einstein crossing time $t_{E,p}$, σ is the fractional precision of each measurement, A_{fs} is the finite-source magnification, and $\tau \equiv (t - t_0)/t_{E,p}$ is the time from the peak of the planetary event in units of the Einstein crossing time. Although we assume the magnification is described by single-lens event with no external shear, our results are approximately applicable to wide-separations planets as well. This is because, as we demonstrate below, planets with mass $m_p \gg M_\oplus$ are detectable with impact parameters $u_{0,p} \geq 1$, where any deviation arising from the caustic induced by the primary will be negligible. On the other hand, for low-mass planets with $\rho_{*,p} \geq 1$, the deviation due to the caustic vanishes up to fourth order in $\rho_{*,p}^{-1}$ when the source completely encloses the caustic (Gould & Gaucherel 1997). Therefore, the isolated point-lens approximation should be sufficient except for a relatively small range near $m_p \sim 0.3 M_\oplus$, where we generally underestimate the S/N .

The top panel of Figure 6 shows the normalized signal-to-noise ratio, $(S/N)/(N^{1/2}/\sigma)$, as a function of the impact parameter u_0 , for source sizes $\rho_{*,p} = 0.0, 2.0, 4.0$ and 6.0 . For small sources, $\rho_{*,p} \ll 1$, and high-magnification events, $u_{0,p} \ll 1$, the term in braces in equation (14) is approximately unity and independent of $u_{0,p}$, and so $S/N \sim N^{1/2}\sigma^{-1}$. In the opposite limit of large impact parameter events, $u_{0,p} \gg 1$, we find

$$\frac{S}{N} = \sqrt{\frac{5\pi N}{4}} \sigma^{-1} u_{0,p}^{-7/2}. \quad (15)$$

The bottom panel of Figure 6 shows the impact parameter $(u_{0,p})_{th}$ for which the S/N is equal to the threshold value $(S/N)_{th} = (1000)^{1/2}$, for the same assumptions adopted in the simulations described in § 3, namely $f_{obs} = 120 \text{ day}^{-1}$,

and $\sigma = 1\%$. This is the appropriate threshold for detecting isolated events in otherwise constant stars (Bennett & Rhee 2002). This critical impact parameter $(u_{0,p})_{th}$ corresponds to the cross section for the detection of a planet of mass m_p . In the small-source, large impact-parameter limit, this can be written

$$(u_{0,p})_{th} \sim 2.3 \left(\frac{m_p}{M_\oplus} \right)^{1/14} \left(\frac{f_{obs}}{120/\text{day}} \right)^{1/7} \times \left(\frac{\sigma}{0.01} \right)^{-2/7} \left[\frac{(S/N)_{th}}{\sqrt{10^3}} \right]^{-2/7}, \quad (16)$$

where f_{obs} is the observational frequency. Therefore, large mass-ratio planetary events can generally be detected with planetary impact parameters significantly larger than unity.

In the limit of large sources $\rho_{*,p} \gg 1$, the magnification is strongly affected by finite source effects. In this case, the lightcurve is reasonably well approximated as a boxcar with a duration $\sim 2t_*$ and an amplitude $A_{fs} \sim 1 + 2\rho_{*,p}^{-2}$ (Di Stefano & Scalzo 1999a; Agol 2003), implying a S/N of,

$$\frac{S}{N} \sim \frac{N^{1/2}}{\sigma} \frac{2^{3/2} \rho_{*,p}^{1/2}}{2 + \rho_{*,p}^2}. \quad (17)$$

Therefore, for a fixed θ_* and μ_{rel} , planets with a mass less than,

$$m_{p,min} \sim 0.02 M_\oplus \left(\frac{f_{obs}}{120/\text{d}} \right) \left(\frac{\sigma}{0.01} \right) \left[\frac{(S/N)_{th}}{\sqrt{10^3}} \right], \quad (18)$$

cannot be detected due to finite source effects. This limit is shown in the bottom panel of Figure 6, and corresponds to roughly a lunar mass, or a mass ratio of $q \sim 2 \times 10^{-7}$ for a primary mass of $\sim 0.3 M_\odot$. Planets with mass ratio larger than this limit, but still well into the finite-source dominated regime, will have a detection cross section of $(u_{0,p})_{th} \sim \rho_{*,p}$, which is generally larger than the corresponding point-source cross section. Therefore, for the parameters we have adopted, the cross section as a function of decreasing q first decreases until $\rho_{*,p} \sim 1$, and then increases until $m_{p,min}$, at which point it suddenly plummets. See Figure 6.

4.2. Mass Measurement

We now estimate the fraction of *detectable* events that yield accurate mass measurements, incorporating our estimate for the cross section for detection from subsection § 4.1. In Figure 7, we plot the boundary of the region in the (m_p, r_\perp) or (q, s) plane where $> 50\%$ of detectable wide-planet events yield a 10% measurement of $\rho_{*,p}$ (thick solid curve). Here we have adopted the analytic form for the cross section to measure $\rho_{*,p}$ to 10% given in equation (13) with $C_\gamma = 2.5$, but normalize to the number of detectable events by dividing the resulting probability by $(u_{0,p})_{th}$. We also show in Figure 7 an approximation to the boundary of the region in the (m_p, r_\perp) or (q, s) plane at which we expect $\sim 50\%$ of detectable events to yield a 10% measurement of $\tilde{r}_{E,p}$ from parallax effects arising from the difference in the lightcurve as seen from a satellite at L2 and a ground-based observer (thick long-dashed curve). Here we have assumed that a planet event detected at a signal-to-noise ratio S/N yields a fractional error in the projected Einstein ring radius of (Gould, Gaudi, & Han 2003; Han et al. 2004),

$$\frac{\sigma_{\tilde{r}_E}}{\tilde{r}_E} \sim \frac{\tilde{r}_{E,p}}{d_{\text{sat}}} \left(\frac{S}{N} \right)^{-1}, \quad (19)$$

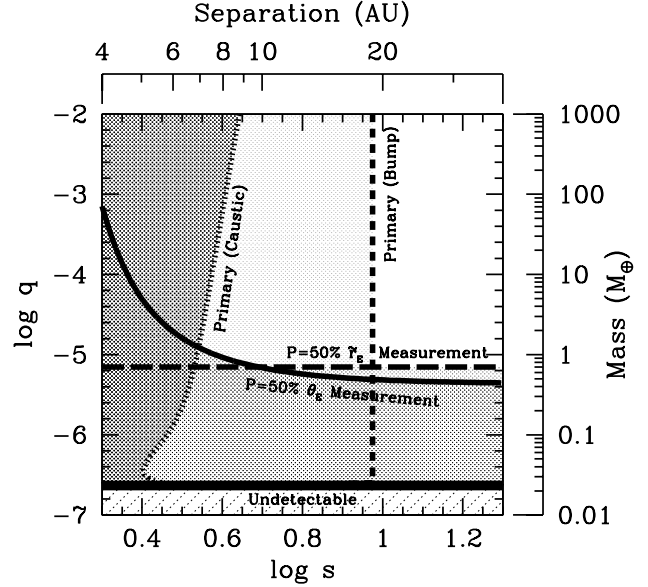


FIG. 7.— Characterization of wide separation planets as a function of the planetary separation s and mass ratio q using a next generation microlensing planet search. The heavy horizontal line shows the lower limit on the mass of detectable planets of $m_p \gtrsim 0.02 M_\oplus$, or $q \gtrsim 2 \times 10^{-7}$. In this figure, planets are considered detected if they produce deviations with signal-to-noise ratio $S/N > (S/N)_{th} = (1000)^{1/2}$. The solid contour is the upper boundary to the region in which $> 50\%$ of detectable planetary events will yield a $\sim 10\%$ measurement of $\rho_{*,p}$. Similarly, the long dashed line is the upper boundary to the region for which $> 50\%$ of detectable planetary events will yield a $\sim 10\%$ measurement of $\tilde{r}_{E,p}$. The dotted contour is the rightmost boundary of the region in which $> 50\%$ of detectable planets can be identified as bound from the deviation caused by the planetary caustic from the nominal point-lens form, where $S/N > (160)^{1/2}$ is required for detection of the deviation. Similarly, the dashed vertical line is the rightmost boundary of the region in which the magnification of primary is detectable for $> 50\%$ of events with $S/N > (160)^{1/2}$. The top and right axes show the conversion from (q, s) to (m_p, r_\perp) assuming a primary mass of $M = 0.3 M_\odot$ and $r_E = 2 \text{ AU}$.

where $d_{\text{sat}} \sim 0.005$ is the projected Earth-satellite separation, and we have assumed our fiducial value of $\pi_{\text{rel}} \simeq 42 \mu\text{as}$, so that $\tilde{r}_{E,p} = 0.024 \text{ AU} (m_p/M_\oplus)^{1/2}$. Here we have ignored the effect of finite sources on the ability to measure $\tilde{r}_{E,p}$. We note that the approximation in equation (19) for the fractional error in $\tilde{r}_{E,p}$ is very crude; however it captures the primary dependence on m_p , and agrees reasonably well with more detailed calculations (Han et al. 2004).

Inspection of Figure 7 indicates that, by combining ground-based observations with those of a satellite in an L2 orbit, it should be possible to measure the mass of a majority of planetary events arising from planets with $m_p \lesssim M_\oplus$, corresponding to $q \lesssim 10^{-5}$, to a fractional precision of $\sim 10\%$. Mass measurements will be possible for a smaller fraction of higher-mass planets. However, since the overall detection rate for such planets will likely be higher, a similar or higher number of reasonably-precise mass measurements may be possible.

4.3. Detection of the Primary

We now consider several methods by which the presence of the primary star can be detected in isolated events caused by wide planets, thus permitting discrimination between bound and isolated planets.

First, as discussed in detail by Han & Kang (2003), it will be possible to identify wide-separation planetary events from the signature of the planetary caustic near the peak of light

curves. Han & Kang (2003) found that the signatures with $\geq 5\%$ deviation can be detected for $\gtrsim 80\%$ of events with $u_{0,p} \leq 1$ caused by Jupiter-mass planets with separations $\lesssim 10$ AU, and the probability is still substantial for separations even up to ~ 20 AU. Here we consider a simplified model for the probability of detecting the primary via the signature of the planetary caustic. We assume that the wide separation can be approximated by a Chang-Refsdal lens. We calculate the fractional deviation δ of the Chang-Refsdal lens from a single lens as a function of position along the two axes of symmetry. We assume that a lightcurve with a peak deviation δ can be distinguished from the single-lens case with a signal-to-noise ratio of

$$\frac{S}{N} \sim \frac{N^{1/2}}{\sigma} (4\gamma)^{1/2} \delta. \quad (20)$$

We then determine the semimajor and semiminor axis of the region around the planetary caustic at which the signal-to-noise ratio is greater than a given threshold $(S/N)_{th}$. The fraction of detectable planetary events for which the primary can be detected via the deviation from a point lens is then given by equation (12) normalized by the cross-section for detection $u_{0,th}$. We choose $(S/N)_{th} = (160)^{1/2}$. This threshold is lower than that assumed for detection of the planetary event because there are fewer lightcurves to search for the deviation arising from the caustic. Figure 7 shows the region in the (q, s) plane where $> 50\%$ of isolated events arising from bound planets give rise to detectable deviations due to the presence of the planetary caustic (thick dotted line). Our results agree well with the results of Han & Kang (2003), when the latter are normalized by $(u_{0,p})_{th}$.

Second, wide-separation planetary events can be distinguished by the additional long-term bumps in the lightcurve caused by the primary star. Compared to the planetary Einstein ring, the Einstein ring of the primary star is much larger, implying a larger effective lensing region. Combined with high precision photometry from space observation, then, the existence of the primary star can often be noticed even without the signatures of the planetary caustic. In the limit of the large impact parameter, u_0 , the “bump” due to the primary can be detected with signal-to-noise ratio given by equation (15). Then, the cross section to detect the primary-induced bump for a given threshold signal-to-noise ratio, $(S/N)_{th}$, is given by

$$P = \begin{cases} 1.0 & \text{for } u_{0,th} > \hat{s}, \\ \frac{2}{\pi} \sin^{-1} \left(\frac{u_{0,th}}{\hat{s}} \right) & \text{for } u_{0,th} < \hat{s}, \end{cases} \quad (21)$$

where $u_{0,th}$ is given by equation (16) with $q = 1$. Figure 7 shows the contour (thick short-dashed line) at which $P = 50\%$ as a function of (s, q) , assuming $(S/N)_{th} = (160)^{1/2}$ and $M = 0.3 M_\odot$. We find that $P = 50\%$ for $s \simeq 9.2$, corresponding to $r_\perp \simeq 18$ AU. It will be possible to detect the primary for essentially all planets with $s \lesssim 6.52$, or $r_\perp \lesssim 13$ AU.

The third method of identifying a wide-separation planet is detecting blended light from the host star. According to Bennett & Rhie (2002), for $\sim 1/3$ of events with detected planets from a space lensing mission, the planetary host star is either brighter than or within ~ 2 magnitudes of the source star’s brightness.

Considering the three methods discussed here together, the prospects for distinguishing isolated planetary events caused by bound and free-floating planets seem good. For roughly $1/3$ of all events, regardless of the mass or separation of the planet, the flux from the primary should be detectable. For $> 1/2$ of all events caused by wide planets with $r_\perp \lesssim 5-9$ AU

(depending on mass), the influence of the primary will be detectable in the lightcurve via the planetary caustic. Finally, $> 1/2$ of all detectable planets with $r_\perp \gtrsim 20$ AU can be inferred to be bound via the low-amplitude bump caused by the magnification of the primary.

5. CONCLUSION

With their excellent photometric precision and extremely high temporal sampling, next-generation microlensing planet searches will be sensitive to planets with masses almost as low as the moon. These searches will employ large-format cameras with large FOV in order to monitor hundreds of millions of stars simultaneously with $\sim 10-20$ minute sampling. Because all stars are monitored continuously regardless of whether they are being lensed or not, such searches will be sensitive to isolated events caused by wide-separation or free-floating planets, in contrast to current microlensing planet searches. Such planets are very difficult or impossible to probe by other planet detection methods.

The scientific return of these wide and free-floating planet detections would be greatly enhanced if their nature could be characterized. In particular, differentiating between wide planets and free-floating objects is highly desirable, as is the measurement of their mass. Generally, the lightcurves of free-floating planets are grossly similar to those of wide-separation planets. Furthermore, microlensing lightcurves generally only yield event time scales, which are degenerate combinations of the mass, distance, and transverse velocity of the lens. However, as recently pointed out by several authors (Gould, Gaudi, & Han 2003; Han & Kang 2003; Han et al. 2004), there are several unique properties of next-generation microlensing surveys that should allow better characterization of wide-separation and free-floating planets. Here we have summarized and built on previous works, addressing the ability of these searches to distinguish wide-separation planets from free-floating planets, as well as to measure planet masses.

We have performed detailed simulations of wide-separation planetary events, and evaluated the probability of measuring the Einstein ring radius θ_E for these events; this is one of the two additional quantities needed to measure the lens mass. From this investigation, we find that the parameter space of the probability distribution is divided into two regimes depending on the ratio between the caustic and normalized source sizes. In the regime in which the source size is much larger than the size of the caustic, the probability is not much different from that of the corresponding free-floating planetary events. In the opposite regime in which the caustic size is much larger than the source size, the probability is significantly higher than the case without the caustic. As a result, the probability of θ_E determination for wide-separation planetary events can be substantially higher than that of free-floating planetary events. We find that the effective cross-section of the caustic is about 1.25 times its linear size.

For the majority of events due to planets with $m_p \leq M_\oplus$, it should be possible to measure the angular Einstein ring radius θ_E to $\sim 10\%$. The projected Einstein ring radius $\tilde{\theta}_E$ should also be measurable to $\sim 10\%$ for the majority of these events by combined observations from the ground and a satellite located in an L2 orbit. Thus, it should be possible to measure the mass of most wide-separation and free-floating planets of Earth-mass or less.

Finally, we have discussed three methods for distinguishing between isolated planetary events caused by free-floating and

bound planets. These include detecting the primary through the influence of the planetary caustic, from the low-amplitude bump in the light curve from the primary, and from detection of the light from the primary itself. These three methods should allow one to distinguish between bound and free-floating planets for $\sim 1/3$ of all events regardless of the planet separation, $> 50\%$ of events with projected separations $\lesssim 20$ AU, and essentially all events with separations $\lesssim 13$ AU.

Center for the Structure and Evolution of the Cosmos (ARC-SEC) of the Korean Science & Engineering Foundation (KOSEF), through the Science Research Center (SRC) program, and by JPL contract 1226901. Work by BSG was supported by the Menzel Fellowship from the Harvard College Observatory. Work by JA was supported by a grant from the Leverhume Trust Foundation. Work by AG was supported by JPL contract 1226901 and NSF grant 02-01266.

Work by CH was supported by Astrophysical Research

REFERENCES

Albrow, M., et al. 1998, *ApJ*, 509, 687
 Alcock, C., et al. 1996, *ApJ*, 463, L67
 Agol, E. 2003, *ApJ*, 594, 449
 Bennett, D.P., & Rhie, S.H. 2002, *ApJ*, 574, 985
 Bond, I.A., et al. 2002, *MNRAS*, 333, 71
 Bond, I.A., et al. 2004, *ApJ*, 606, L155
 Chang, K., & Refsdal, S. 1979, *Nature*, 282, 561
 Chang, K., & Refsdal, S. 1984, *A&A*, 132, 168
 Di Stefano, R., & Scalzo, R.A. 1999, *ApJ*, 512, 564
 Di Stefano, R., & Scalzo, R.A. 1999, *ApJ*, 512, 579
 Dominik, M. 1998, *A&A*, 333, L79
 Dominik, M. 1999, *A&A*, 349, 108
 Gaudi, B.S., Han, C., & Gould, A. 2004, in preparation
 Gould, A., & Gaucherel, C. 1997, *ApJ*, 477, 580
 Gould, A., Gaudi, B.S., & Han, C. 2003, *ApJ*, 591, L53
 Gould, A., & Loeb, A. 1992, *ApJ*, 396, 104
 Gould, A., & Welch, D.L. 1996, *ApJ*, 464, 212
 Griest, K., & Safizadeh, N. 1998, *ApJ*, 500, 37
 Han, C., & Kang, Y.W. 2003, *ApJ*, 596, 1320
 Han, C., Chung, S.-J., Kim, D., Park, B.-G., Ryu, Y.-H., Kang, S., & Lee, D. W. 2004, *ApJ*, 604, 372
 Holtzman, J.A., Watson, A.M., Baum, W.A., Grillmair, C.J., Groth, E.J., Light, R.M., Lynds, R., & O'Neil Jr., E.J. 1998, *AJ*, 115, 1946
 Mao, S., & Paczyński, B. 1991, *ApJ*, 374, L37
 Paczyński, B. 1986, *ApJ*, 304, 1
 Rhie, S.H., et al. 2000, *ApJ*, 533, 378
 Udalski, I., et al. 2001, *ApJ*, 552, 731
 van Belle, G.T. 1999, *PASP*, 111, 1515
 Witt, H.J. 1990, *A&A*, 236, 311
 Witt, H.J., & Mao, S. 1995, *ApJ*, 447, L105
 Yoo, J., et al. 2004a, *ApJ*, 603, 139
 Yoo, J., et al. 2004b, *ApJ*, submitted (astro-ph/0403459)